Enceladus's internal ocean and ice shell constrained from Cassini gravity, shape, and libration data

Ondřej Čadek, G. Tobie, Tim Van hoolst, Marion Massé, Gael Choblet, Axel Lefèvre, Giuseppe Mitri, Rose-Marie Baland, Marie Běhounková, Olivier Bourgeois, et al.

AGU PUBLICATIONS

Geophysical Research Letters

RESEARCH LETTER
10.1002/2016GL068634

Key Points:
- Gravity, shape, and libration data can be satisfied by models with a 200–400 m elastic lithosphere
- The ice shell has a variable thickness, 20 km on average and smaller than 5 km at the South Pole
- Best fit models require an ocean density of at least 1030 kg/m^3 and a core radius of 180–185 km

Supporting Information:
- Supporting Information S1
- Text S1
- Figure S1
- Figure S2

Correspondence to:
O. Čadek,
oc@karel.troja.mff.cuni.cz

Citation:
Čadek, O., et al. (2016), Enceladus's internal ocean and ice shell constrained from Cassini gravity, shape, and libration data, *Geophys. Res. Lett.*, *43*, 5653–5660, doi:10.1002/2016GL068634.

Received 9 MAR 2016
Accepted 17 MAY 2016
Accepted article online 23 MAY 2016
Published online 11 JUN 2016

Enceladus's internal ocean and ice shell constrained from Cassini gravity, shape, and libration data

Ondřej Čadek[1], Gabriel Tobie[2], Tim Van Hoolst[3,4], Marion Massé[2], Gaël Choblet[2], Axel Lefèvre[2], Giuseppe Mitri[2], Rose-Marie Baland[3], Marie Běhounková[1], Olivier Bourgeois[2], and Anthony Trinh[3]

[1]Department of Geophysics, Faculty of Mathematics and Physics, Charles University in Prague, Prague 8, Czech Republic, [2]Laboratoire de Planétologie et Géodynamique, UMR-CNRS, University of Nantes, Nantes, France, [3]Royal Observatory of Belgium, Brussels, Belgium, [4]Instituut voor Sterrenkunde, KU Leuven, Leuven, Belgium

Abstract The intense plume activity at the South Pole of Enceladus together with the recent detection of libration hints at an internal water ocean underneath the outer ice shell. However, the interpretation of gravity, shape, and libration data leads to contradicting results regarding the depth of ocean/ice interface and the total volume of the ocean. Here we develop an interior structure model consisting of a rocky core, an internal ocean, and an ice shell, which satisfies simultaneously the gravity, shape, and libration data. We show that the data can be reconciled by considering isostatic compensation including the effect of a few hundred meter thick elastic lithosphere. Our model predicts that the core radius is 180–185 km, the ocean density is at least 1030 kg/m^3, and the ice shell is 18–22 km thick on average. The ice thicknesses are reduced at poles decreasing to less than 5 km in the south polar region.

1. Introduction

Since the discovery of a surprising plume activity at Enceladus's South Pole [*Porco et al.*, 2006; *Hansen et al.*, 2006; *Waite et al.*, 2006; *Spencer et al.*, 2006], a series of geophysical evidence has hinted at the presence of a liquid water reservoir beneath the ice shell [*Collins and Goodman*, 2007; *Nimmo et al.*, 2007; *Tobie et al.*, 2008; *Iess et al.*, 2014; *Běhounková et al.*, 2015]. The detection of sodium and potassium salts in icy grains emanating from Enceladus's south polar faults [*Postberg et al.*, 2009, 2011] suggests that the plume source is most likely connected to a subsurface saltwater reservoir. The recent discovery of silicon-rich particles further indicates that hydrothermal interactions are currently occurring at the base of the ocean and that hydrothermal products are quickly transported to the plume source [*Hsu et al.*, 2015]. However, the extent and location of the subsurface liquid reservoir as well as the way it is connected to the jet source at the surface remain unconstrained.

Based on the global shape data which show a topographic depression at the South Pole [*Thomas et al.*, 2007], it has long been proposed that the liquid reservoir may be located only in the Southern Hemisphere [*Collins and Goodman*, 2007], thus explaining why the activity is concentrated around the South Pole [*Tobie et al.*, 2008]. First interpretation of the topography and gravity data [*Iess et al.*, 2014; *McKinnon*, 2015] suggests that the ice shell is about 30 to 40 km thick at the South Pole, and its thickness increases to about 60 km in the equatorial region. However, from these data alone, it is not possible to definitively conclude whether the ocean is global or only located in the Southern Hemisphere. More recently, the detection of a significant physical libration [*Thomas et al.*, 2016] has indicated that the ice shell is mechanically decoupled from the rocky core, thus providing the first direct evidence for a global subsurface ocean. *Thomas et al.* [2016] have showed that the observed libration is consistent with an average ice shell thickness of 21–26 km, which is significantly less than the value predicted from gravity and topography.

In order to provide further constraints on the ice/ocean configuration as well as on the thermal state and composition of the interior, we develop in the present study an interior structure model consisting of a rocky core, an internal ocean, and an ice shell of variable thickness which simultaneously satisfies the observed gravity, shape, and libration data, and we compare the modeled ice shell structure with the major geological units. Details on our modeling approach are provided in section 2. By performing a systematic exploration of the parameter space, we determine, in section 3, the structures which provide the best fit to the available

geophysical data. Finally, in section 4, we discuss the implications of our results for the geological and thermal history of Enceladus.

2. Method Description

2.1. Model Assumptions

We assume that the moon consists of three homogeneous domains: the core of density ρ_1, the water ocean of density ρ_2, and the solid ice crust of density ρ_3. The boundaries of the domains are generally aspherical and their shapes are described by radius functions $r_i(\theta, \phi)$, where θ is the colatitude, ϕ is the longitude, and indices $i = 1, 2, 3$ refer to the core-ocean boundary, liquid water-solid ice boundary, and the surface of the moon, respectively. The mean radii of the interfaces are $R_i = (4\pi)^{-1} \int_\Omega r_i \mathrm{d}\Omega$, where Ω denotes the surface of the sphere. To describe the surface, r_3, we use the long-wavelength model of *Nimmo et al.* [2011], which has been derived from limb profiles in terms of a spherical harmonic series truncated at degree 8. The density of ice is fixed at a value $\rho_3 = 925$ kg m^{-3}. For the ocean layer, we consider density values ranging from 1007 to 1050 kg m^{-3}. The density of the core depends on the choice of parameters R_1 and R_2 and is determined from the total mass M of the moon, $M = 1.08022 \times 10^{20}$ kg.

As shown by *Iess et al.* [2014], Enceladus is not in hydrostatic equilibrium. The topography of the satellite, defined as $r_3 - h_3$, where h_3 is the equipotential surface with mean radius R_3, is nonzero, and therefore, it must be maintained either by elastic support, isostasy, and/or dynamical processes in the ice shell. In the present study, we compute the combined effect of elastic support and isostasy associated with ice shell thickness variations to determine the ice/ocean structure compatible with the available observations. We neglect the possible effect of dynamic topography and any lateral density variations due to temperature and porosity anomalies within the ice shell. The relationship between the surface and ice/ocean topography then reads

$$C_{\mathrm{el}}\rho_3(r_3 - h_3)g_3R_3^2 + (\rho_2 - \rho_3)(r_2 - h_2)g_2R_2^2 = 0, \tag{1}$$

where g_2 and g_3 are the mean values of the gravitational acceleration at radii R_2 and R_3, respectively, and h_2 is the equipotential surface with mean radius R_2. Parameter C_{el} characterizes the effect of elastic flexure, $C_{\mathrm{el}} \in \langle 0, 1 \rangle$, and generally increases with the effective elastic thickness T_e. In a first approach, we assume that T_e does not vary laterally which allows us to use the spectral equation (25) in *Kalousová et al.* [2012]. This equation is identical to equation (27) in *Turcotte et al.* [1981] in which mantle density ρ_m is set to ρ_3, crustal density ρ_c is set to zero and the terms with average density $\bar{\rho}$ are omitted. The value of C_{el} we obtain in the present study typically varies between 0.75 and 0.9. We assume that the core is in hydrostatic equilibrium, namely, $r_1 = h_1$, where function h_1 describes the shape of the equipotential surface with mean radius R_1. The validity of this assumption may be questionable (see discussion in *McKinnon* [2015]), but it is indirectly supported by the previous studies by *Iess et al.* [2014] and *McKinnon* [2015] which have indicated that no strong core deflections are needed to explain the topography and gravity data and which is further confirmed by the analysis presented here.

2.2. Computation of Equipotential Surfaces

For each interface $i = 1, 2, 3$, the equipotential surface, $h_i(\theta, \phi)$, is computed such that the sum of gravitational potential V and static tidal potential W remains constant along the surface:

$$V(h_i, \theta, \phi) + W(h_i, \theta, \phi) = \text{constant} \tag{2}$$

Using the standard expression for tidal potential W [e.g., *Kaula*, 1964],

$$W(r, \theta, \phi) = r^2\omega^2 \left[\frac{1}{3} - \frac{5}{6}P_{20}(\cos\theta) + \frac{1}{4}P_{22}(\cos\theta)\cos 2\phi\right] \equiv r^2\omega^2\psi(\theta, \phi), \tag{3}$$

applying the Taylor series expansion around R_i and assuming $|h_i - R_i|^2 \ll R_i^2$, equation (2) can be rewritten as follows:

$$V_i(\theta, \phi) - g_i(h_i - R_i) + \left[R_i^2 + 2R_i(h_i - R_i)\right]\omega^2\psi(\theta, \phi) = \text{const}, \tag{4}$$

where V_i and g_i are the variations of the gravitational potential and the mean value of the gravitational acceleration at radius R_i, respectively, ω is the angular velocity, and P_{20} and P_{22} in equation (3) are the associated Legendre functions.

Since the ice crust, the water ocean and the core are assumed to be homogeneous; the gravitational potential V_i is a sum of potentials generated by deflections of the surface and the internal density interfaces:

$$V_i = \left[V_{r_1} + V_{r_2} + V_{r_3}\right]_{r=R_i}, \tag{5}$$

where potentials $V_{r_k}, k = 1, 2, 3$, are computed exactly using general formulas for gravitational potential of topographic loads [e.g., *Martinec*, 1994]. Compared to the simplified linearized approximation, the use of exact formulas leads to a difference of about 20% in the prediction of the surface potential.

2.3. Comparison With Observed Gravitational Coefficients

Our goal is to determine the values of radii R_1 and R_2 that best predict the observed gravitational signal. We consider several models with different values of ocean density ρ_2 (ranging from 1007 to 1050 kg m^{-3}) and effective elastic thickness T_e (0–500 m). For each set of parameters ρ_2, T_e, R_1, and R_2 (and fixed values of M and ρ_3) we determine the core density ρ_1 and compute the shapes of the internal density interfaces (r_1 and r_2) and the gravitational potential V_3. For the low degrees (2 and 3), we then compare the computed potential coefficients with the values constrained by Cassini measurements [*Iess et al.*, 2014] in order to determine the values of parameters R_1 and R_2 that minimize the misfit between the observed and predicted gravitational potential:

$$S(R_1, R_2) = \sum_{\ell=2}^{3} \left(\frac{C_{\ell 0}^{\mathrm{obs}} - C_{\ell 0}^{\mathrm{pred}}}{\sigma_{\ell 0}} \right)^2 + \left(\frac{C_{22}^{\mathrm{obs}} - C_{22}^{\mathrm{pred}}}{\sigma_{22}} \right)^2, \tag{6}$$

where $C_{\ell m}^{\mathrm{pred}}$ are the coefficients of the gravitational potential predicted for parameters R_1 and R_2, and $C_{\ell m}^{\mathrm{obs}}$ are the spherical harmonic coefficients of the observed gravitational potential [*Iess et al.*, 2014] obtained with formal errors $\sigma_{\ell m}$ (we note that the solution of the inversion does not change significantly if $\sigma_{\ell m}$ are replaced by 1). The inverse problem (6) is solved by a systematic exploration of all admissible combinations of parameters R_1 and R_2, i.e., by repeated solution of equations (1), (4), and (5) in the spectral domain. Due to the product $h_i\psi$ of two laterally dependent functions in equation (4) and the nonlinear nature of equation (5), these equations cannot be classified according to order and degree. As a consequence, the gravitational potential predicted at a given degree and order generally depends on topographic coefficients at all other degrees and orders. The topography is considered up to degree 8, and equations (1), (4), and (5) are solved up to degree 16.

2.4. Computation of Physical Libration

For the interior structure parameters that lead to the minimum misfit between observed and predicted data, we then compute the libration using the degree 2 shape of each interface. As Enceladus is in 1:1 spin-orbit resonance in which its long axis is oriented toward the empty focus of the orbit and not to Saturn, the planet exerts a gravitational torque on the Moon. As a result, the rotation of Enceladus changes with a period equal to the orbital period. The amplitude of libration determined by *Thomas et al.* [2016] is (528 ± 62) m. To evaluate libration amplitudes for our best fit structural models, we solve the equations governing the libration of an icy satellite with a global subsurface ocean in synchronous rotation about its central planet [*Van Hoolst et al.*, 2013, equations (45) and (46)]. In this method, the changes in angular momentum of the shell, ocean, and core are calculated from the torques applied to the layers. Besides the gravitational torques exerted by Saturn on the ice shell, ocean, and solid core, the method takes into account the gravitational torques exerted by the internal layers on each other and the pressure torques exerted by the ocean on the shell and the core. It also includes additional torques related to the periodic tidal deformations. We adapt the method developed for satellites in hydrostatic equilibrium to nonhydrostatic equilibrium by adding differences between the torques on the nonhydrostatic structure and on the structure for Enceladus in hydrostatic equilibrium. The libration amplitude moderately depends on the ice shell rigidity, with a variation of about 50 m (just below the observational uncertainty) for rigidity values between 10^9 Pa and 5×10^9 Pa, and it is almost insensitive to the core rigidity. Ice viscosity reduces the libration amplitude, but the reduction is well below the observational uncertainty, with values up to 20 m for ice viscosities in the bottom part of the ice shell below 10^{13} Pa s [*Van Hoolst et al.*, 2016].

3. Best Fit Solutions: Influence of Effective Elastic Thickness and Ocean Density

Following the procedure described in section 2, we compute the shape of the bottom ice shell interface by systematically exploring all admissible combinations of parameters R_1, R_2, and T_e. The shape of the interface is determined for ice density $\rho_1 = 925$ kg m^{-3} and three different values of ocean density ρ_2, corresponding to

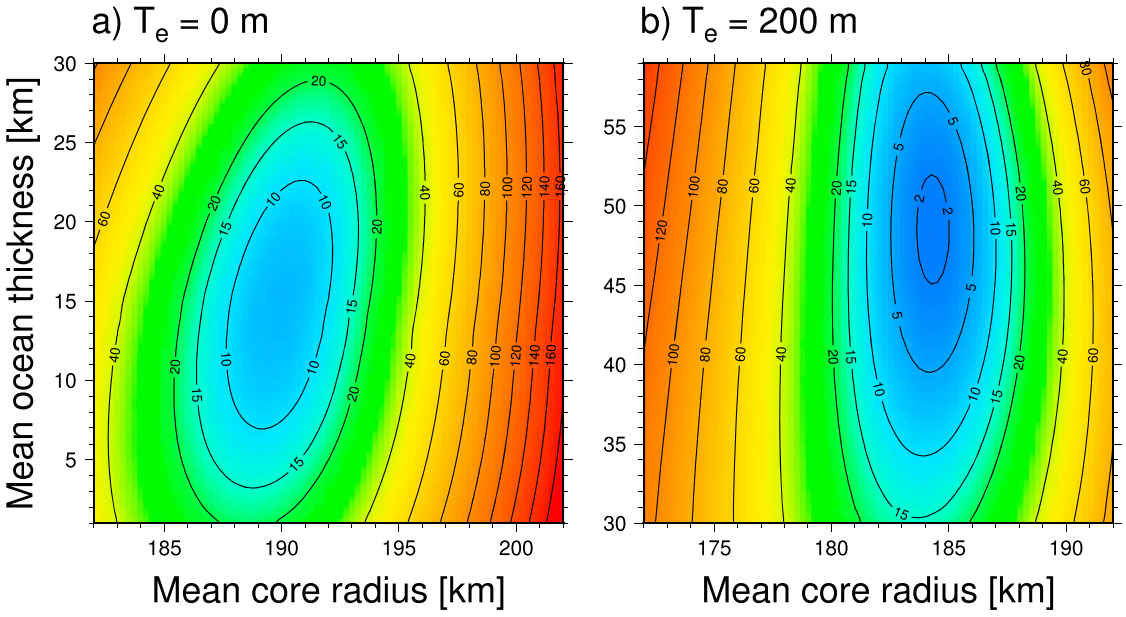

Figure 1. Misfit between observed and predicted gravitational potential coefficients (equation (6)) as a function of mean ocean thickness and core radius, obtained for models with (a) no elastic layer and with (b) a 200 m elastic lithosphere. The calculation is carried out for an ocean density of 1030 kg m^{-3} and ice shell density of 925 kg m^{-3}. The results for models with ocean density of 1007 and 1050 kg m^{-3} are provided in the supporting information.

different salinity values. Figure 1 presents the misfit between the computed and observed gravitational potential (equation (6)) obtained for $\rho_2 = 1030$ kg m^{-3} and for two end-members of T_e: one with no elastic support ($T_e = 0$) and the other with a 200 m thick elastic lithosphere. The models with no elastic support (Figure 1a) give the best fit for an average ice shell thickness of 45–50 km, consistent with the interpretation of *Iess et al.* [2014] and *McKinnon* [2015] but much larger than the value expected from the observed physical libration [*Thomas et al.*, 2016]. Including the elastic flexure of the upper part of the ice shell results in the reduction of the average ice shell thickness (Figure 1b). The shape of the misfit functions indicates that the core radius (R_1) can be determined with the accuracy of a few kilometers. The uncertainty in determining the radius of the ice/ocean interface (R_2) is significantly larger, and the average ice shell thickness in models that reasonably fit the data ($S < 10$) may differ by more than 10 km.

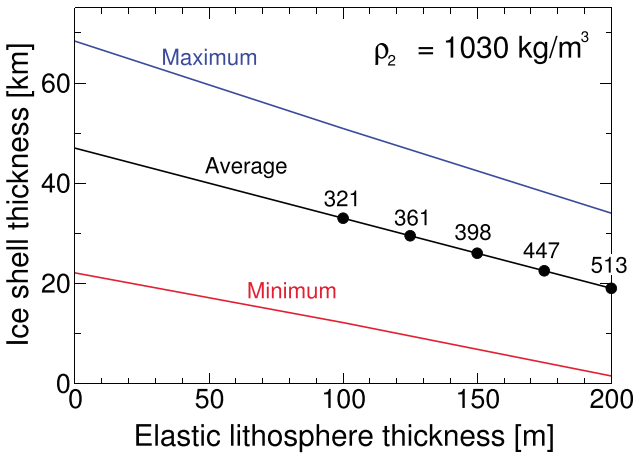

Figure 2. Average (black), minimum (red), and maximum (blue) ice shell thickness for the best fit solutions plotted as a function of elastic thickness T_e. The labels above the black solid circle indicate the amplitudes of libration in meter, predicted for selected models. The curves have been obtained for an ocean density of 1030 kg m^{-3}. The results for models with ocean density of 1007 and 1050 kg m^{-3} are provided in the supporting information.

As illustrated in Figure 2, the average, minimum, and maximum values of ice shell thickness for the best fit models vary almost linearly with elastic thickness T_e. Similar trends are obtained also for ocean densities 1007 and 1050 kg m^{-3} (Figures S1 and S2 in the supporting information). A libration amplitude consistent with the observed libration can be found only for $T_e \geq 175$ m, corresponding to an average ice shell thickness smaller than 21 km. For models with lower ocean density (1007 kg m^{-3}, Figure S2a), no models satisfying the libration constraint can be found. The only way to get a model satisfying the libration would be to further reduce the average ice shell thickness

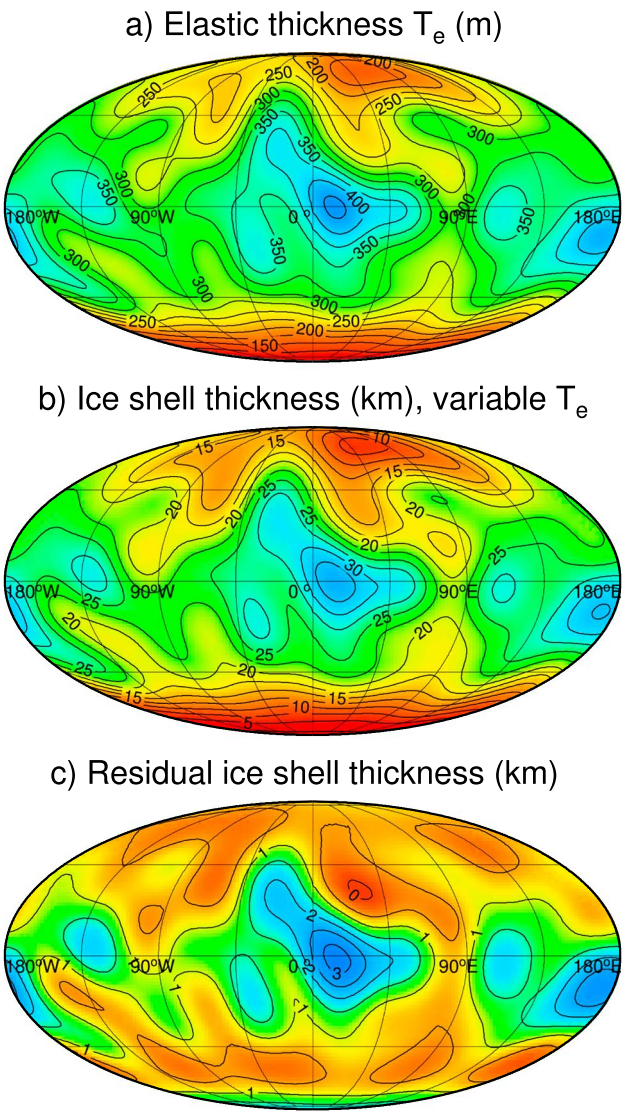

Figure 3. Map of variable elastic layer T_e (a) and corresponding total ice shell thickness (b). Panel c shows the difference between the ice shell thickness obtained for a model with constant T_e = 175 m and that plotted in panel b. All maps have been obtained for an ocean density of 1030 kg m^{-3}.

by increasing the elastic thickness above 200 m, which is not possible as the ice shell at the South Pole gets below zero for T_e = 200 m. By contrast, increasing the ocean density to 1050 kg m^{-3} (Figure S2b) increases the number of acceptable models. For ocean densities between 1030 and 1050 kg m^{-3}, acceptable models have an average ice shell thickness between 18 and 22 km, corresponding to a minimum thickness at the South Pole ranging from 1.5 to 5 km, respectively.

For a selected set of models, we have also tested the influence of variable elastic thickness. The model with variable T_e is derived iteratively from the best fitting model obtained for a constant elastic thickness by gradually increasing T_e in regions of large crustal thickness and decreasing it elsewhere. At each iterative step the parameters R_1 and R_2 are modified by minimizing the misfit function (6). The elastic flexure for models with laterally variable T_e is computed using the approximate formula (42) in *Kalousová et al.* [2012], including compressibility and self-gravitation. As the solution with varying thickness is nonunique, the procedure is somewhat arbitrary. Its main purpose is to test whether the ice shell structure obtained for constant T_e may be significantly influenced by lateral variations. Figure 3 shows the map of ice shell thickness (Figure 3b) obtained for an elastic thickness varying linearly with total ice thickness (Figure 3a). Figure 3c illustrates the difference between the ice shell thickness obtained for a model with a constant elastic thickness of 175 m and that computed for laterally variable T_e shown in Figure 3b. These two models result in comparable ice shell structures; for the case with variable T_e, the difference between the minimum and maximum thicknesses is just slightly reduced compared to the case with constant T_e. The main difference between the two models is the average radius of the rocky core which is 180 and 185 km, respectively. This corresponds to a slightly different ocean volume varying between 25.1 and 26.6 millions of cubic kilometers.

4. Implications for Geological and Thermal History of Enceladus

As illustrated in Figure 4, the reduced ice thickness predicted by our model at the South Pole correlates well with the central south polar terrain (SPT), with a progressive ice shell thickening outside this region. Remarkably, a reduction of the ice shell thickness is also predicted in the north polar terrain, though less pronounced. The North Pole is dominated by cratered plains, and it is obviously less active than the South Pole (for definition of tectonic units, see *Crow-Willard and Pappalardo* [2015]). However, the regions where

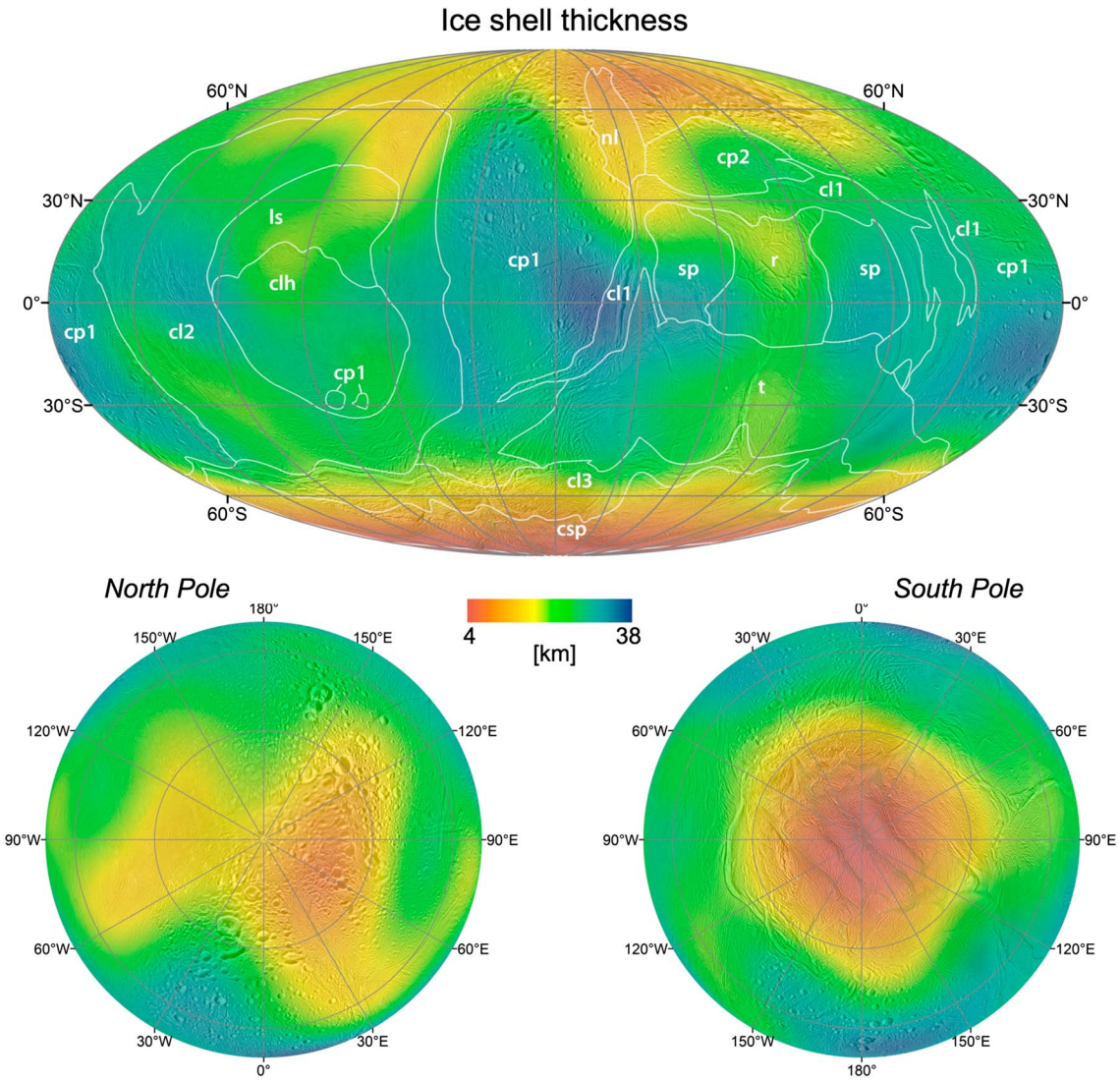

Figure 4. Map of ice shell thickness for the best fit solution with an ocean density of 1030 kg m^{-3} and an effective elastic layer of 200 m (similar to that in Figure 3c), plotted over Cassini imaging mosaic [*Schenk*, 2014] highlighting the main geological units of Enceladus as defined by *Crow-Willard and Pappalardo* [2015].

the minimum thickness is predicted appear to coincide with regions affected by the most recent activity. In particular, the thinnest part of the ice shell correlates relatively well with the northern lineated terrain at longitude around 30°E and latitude between ~50 and 80°N, characterized in its eastern part by truncated, tectonically modified craters.

Some remarkable correlations are also found in the equatorial region, especially in the trailing hemisphere terrain. The striated plains, which are interpreted as the oldest tectonized terrain in this area [*Crow-Willard and Pappalardo*, 2015], appear to coincide with a thickening of the ice shell, while the more recent prominent scarp of Labtayt Sulci, extending from the edge of the SPT to the equator at ~70°E, and the ridged terrains are located within the thinnest part of the ice shell in this area. In the leading hemisphere, the boundary between the older cratered plains and the younger curvilinear terrains coincides with a rapid increase of the ice shell thickness although the overall correlation is not as straightforward.

Possible lateral density variations due to porosity [e.g., *Besserer et al.*, 2013] might affect the topography interpretation in term of ice shell thickness, making the correlation between ice shell thickness and geological units more complex. However, this should mostly affect the oldest terrains where the presence of a kilometric

porous layer is more likely but should not influence the ice shell thickness in the youngest terrains. An elastic thickness ranging typically between 150 and 300 m is consistent in the SPT with the recent estimate of *Bland et al.* [2015] obtained from numerical modeling of funiscular plains formation, as well as with the widespread presence of viscously relaxed craters.

If our analysis is correct, it completely changes our view of Enceladus's present-day thermal state and its recent evolution. The ice shell structure we inferred implies a very strong heat source in the interior, with a focusing mechanism at the South Pole. For an ice shell thickness varying between 1.5 and 3 km, the heat loss by only thermal diffusion would vary between 200 and 400 mW m^{-2}, implying either a strong dissipation in the ice shell or in the deep interior. The global heat loss in our models is estimated to be 25–30 GW, with about 3–5 GW of diffusive heat loss in the SPT, which, although much thinner, contributes by less than 7% to the entire surface. Another issue concerns the mechanical stability of the strongly deflected ocean/ice interface. By modeling the mechanical relaxation of the ice shell structure following the approach of *Lefevre et al.* [2014], we find that the relaxation velocity remains smaller than a few centimeters per year only if the ice shell is conductive with a bottom viscosity of at least $10^{14} - 10^{15}$ Pa s. This implies a weak tidal dissipation in most of the ice shell, except in the SPT.

Due to the small size of Enceladus, the amplitude of tidal deformation is very sensitive to the ice shell thickness, which contrasts with big moons like Europa or Titan, where tidal deformation only slightly depends on ice shell thickness [e.g., *Tobie et al.*, 2005]. As a consequence, the shell thinning in the SPT results in a significant increase of tidal strain [*Čadek et al.*, 2015], enhancing tidal heating due to viscous and shear friction along the main faults. For viscosity between 10^{13} and 10^{14} Pa s, optimal tidal heating is found for ice shell thickness between 1 and 3.5 km, corresponding to the typical thickness in the SPT (Figure 3b). Tidal heat flow ranging between 150 and 500 mW m^{-2} can be generated in the warm and thin SPT, while, outside the SPT, tidal heating in the conductive ice shell would barely exceed 5–10 mW m^{-2}, too weak to counterbalance the diffusive heat loss.

Such a configuration implies either that the ocean is presently crystallizing, with maximum crystallization rates in the equatorial regions due to low tidal heat production, or that the core releases a large amount of heat to counterbalance the heat loss. The first option suggests that tidal heating was even more powerful in a recent past, probably due to higher eccentricity [e.g., *Běhounková et al.*, 2012], allowing the formation of a very thin ice shell which is now growing. The second option implies a very efficient dissipation process in the interior, possibly in an unconsolidated core as proposed by *Roberts* [2015] or in the ocean [e.g., *Tyler*, 2011]. However, it is still unclear whether dissipation in a water-saturated porous core and heat transport through the ocean could explain the present-day structure. These options are not exclusive and are consistent with the latest estimates of the dissipation function in Saturn [*Lainey et al.*, 2012, 2015], which indicates that a strong dissipation may be sustained during relatively long periods of time before the orbital eccentricity would be damped. A strong dissipation in the core may also provide the energy source to power the hydrothermal activity as suggested by the detection of nanosilica emitted from Enceladus [*Hsu et al.*, 2015] and to sustain long-term circulation of hot water in the core as modeled by *Travis and Schubert* [2015].

5. Conclusion

We show that the available topography, gravity, and libration data can be reconciled by considering the isostatic compensation of the surface topograhy including the effect of a few hundred meter thick elastic lithosphere. Our analysis suggests that the low-degree gravity field and libration can be reproduced only by a limited set of model parameters. Our results imply an ocean density of about 1030 kg m^{-3}, compatible with inferred oceanic salinity [*Zolotov*, 2007; *Postberg et al.*, 2009, 2011]. The total ocean volume is estimated to about 40% of the total volume, which is comparable to the rocky core volume. We predict an ice shell thickness ranging between 2 and 5 km in the SPT as well as a thinning of the ice shell around the North Pole, although less pronounced, suggesting the possibility of recent activity. This indicates that the shallow ocean interface could be mapped in the polar terrains, especially at the South Pole, using ice-penetrating radar in future exploration missions. Moreover, accurate measurements of the gravity field at higher harmonic degrees will allow us to further constrain the compensation mechanisms and the ice shell structure in term of ice shell and elastic lithosphere thickness. Such measurements would provide crucial constraints on the thermal state of Enceladus's interior and its present-day heat source, which, along with compositional information from plume sampling, are essential to address the astrobiological potential of this fascinating Moon.

Acknowledgments
The authors thank James Roberts and William B. Moore for the constructive comments that helped to improve the manuscript. The research leading to these results has received financial support from the European Research Council under the European Community's Seventh Framework Programme FP7/2007-2013, grant agreement 259285 (G.T., G.C., and A.L.) and from the Région Pays de la Loire—Connect Talent JUPILOIRE (M.M. and G.M.).

References

Běhounková, M., G. Tobie, G. Choblet, and O. Čadek (2012), Tidally-induced melting events as the origin of South-Pole activity on Enceladus, *Icarus*, *219*, 655–664, doi:10.1016/j.icarus.2012.03.024.
Běhounková, M., G. Tobie, O. Čadek, G. Choblet, C. Porco, and F. Nimmo (2015), Timing of water plume eruptions on Enceladus explained by interior viscosity structure, *Nat. Geosci.*, *8*, 601–604, doi:10.1038/ngeo2475.
Besserer, J., F. Nimmo, J. H. Roberts, and R. T. Pappalardo (2013), Convection-driven compaction as a possible origin of Enceladus's long wavelength topography, *J. Geophys. Res. Planets*, *118*, 908–915, doi:10.1002/jgre.20079.
Bland, M. T., W. B. McKinnon, and P. M. Schenk (2015), Constraining the heat flux between Enceladus' tiger stripes: Numerical modeling of funiscular plains formation, *Icarus*, *260*, 232–245, doi:10.1016/j.icarus.2015.07.016.
Čadek, O., G. Choblet, M. Běhounková, G. Tobie, and T. Kozubek (2015), Effect of ice-shell thickness variations on the tidal deformation of Enceladus, Abstracts #P11D-06 presented at 2015 Fall Meeting, AGU.
Collins, G. C., and J. C. Goodman (2007), Enceladus' south polar sea, *Icarus*, *189*, 72–82, doi:10.1016/j.icarus.2007.01.010.
Crow-Willard, E. N., and R. T. Pappalardo (2015), Structural mapping of Enceladus and implications for formation of tectonized regions, *J. Geophys. Res. Planets*, *120*, 928–950, doi:10.1002/2015JE004818.
Hansen, C. J., L. Esposito, A. I. F. Stewart, J. Colwell, A. Hendrix, W. Pryor, D. Shemansky, and R. West (2006), Enceladus' water vapor plume, *Science*, *311*, 1422–1425, doi:10.1126/science.1121254.
Hsu, H.-W., et al. (2015), Ongoing hydrothermal activities within Enceladus, *Nature*, *519*, 207–210, doi:10.1038/nature14262.
Iess, L., et al. (2014), The gravity field and interior structure of Enceladus, *Science*, *344*, 78–80, doi:10.1126/science.1250551.
Kalousová, K., O. Souček, and O. Čadek (2012), Deformation of an elastic shell with variable thickness: A comparison of different methods, *Geophys. J. Int.*, *190*, 726–744, doi:10.1111/j.1365-246X.2012.05539.x.
Kaula, W. M. (1964), Tidal dissipation by solid friction and the resulting orbital evolution, *Rev. Geophys.*, *2*, 661–685, doi:10.1029/RG002i004p00661.
Lainey, V., et al. (2012), Strong tidal dissipation in Saturn and constraints on Enceladus' thermal state from astrometry, *Astroph. J.*, *752*, 14, doi:10.1088/0004-637X/752/1/14.
Lainey, V., et al. (2015), New constraints on Saturn's interior from Cassini astrometric data, *ArXiv e-prints*.
Lefevre, A., G. Tobie, G. Choblet, and O. Čadek (2014), Structure and dynamics of Titan's outer icy shell constrained from Cassini data, *Icarus*, *237*, 16–18, doi:10.1016/j.icarus.2014.04.006.
Martinec, Z. (1994), The density contrast at the Mohorovicic discontinuity, *Geophys. J. Int.*, *117*, 539–544, doi:10.1111/j.1365-246X.1994.tb03950.x.
McKinnon, W. B. (2015), Effect of Enceladus's rapid synchronous spin on interpretation of Cassini gravity, *Geophys. Res. Lett.*, *42*, 2137–2143, doi:10.1002/2015GL063384.
Nimmo, F., J. R. Spencer, R. T. Pappalardo, and M. E. Mullen (2007), Shear heating as the origin of the plumes and heat flux on Enceladus, *Nature*, *447*, 289–291, doi:10.1038/nature05783.
Nimmo, F., B. G. Bills, and P. C. Thomas (2011), Geophysical implications of the long-wavelength topography of the Saturnian satellites, *J. Geophys. Res.*, *116*, E11001, doi:10.1029/2011JE003835.
Porco, C. C., et al. (2006), Cassini observes the active South Pole of Enceladus, *Science*, *311*, 1393–1401, doi:10.1126/science.1123013.
Postberg, F., S. Kempf, J. Schmidt, N. Brilliantov, A. Beinsen, B. Abel, U. Buck, and R. Srama (2009), Sodium salts in E-ring ice grains from an ocean below the surface of Enceladus, *Nature*, *459*, 1098–1101, doi:10.1038/nature08046.
Postberg, F., J. Schmidt, J. Hillier, S. Kempf, and R. Srama (2011), A salt-water reservoir as the source of a compositionally stratified plume on Enceladus, *Nature*, *474*, 620–622, doi:10.1038/nature10175.
Roberts, J. H. (2015), The fluffy core of Enceladus, *Icarus*, *258*, 54–66, doi:10.1016/j.icarus.2015.05.033.
Schenk, P. (2014), The colors of Enceladus: From plumes and particles to active fractures, paper presented at 45th Lunar and Planetary Science Conference, Lunar 2618.
Spencer, J. R., J. C. Pearl, M. Segura, F. M. Flasar, A. Mamoutkine, P. Romani, B. J. Buratti, A. R. Hendrix, L. J. Spilker, and R. M. C. Lopes (2006), Cassini encounters Enceladus: Background and the discovery of a south polar hot spot, *Science*, *311*, 1401–1405, doi:10.1126/science.1121661.
Thomas, P. C., et al. (2007), Shapes of the saturnian icy satellites and their significance, *Icarus*, *190*, 573–584, doi:10.1016/j.icarus.2007.03.012.
Thomas, P. C., R. Tajeddine, M. S. Tiscareno, J. A. Burns, J. Joseph, T. J. Loredo, P. Helfenstein, and C. Porco (2016), Enceladus's measured physical libration requires a global subsurface ocean, *Icarus*, *264*, 37–47, doi:10.1016/j.icarus.2015.08.037.
Tobie, G., A. Mocquet, and C. Sotin (2005), Tidal dissipation within large icy satellites: Applications to Europa and Titan, *Icarus*, *177*, 534–549, doi:10.1016/j.icarus.2005.04.006.
Tobie, G., O. Čadek, and C. Sotin (2008), Solid tidal friction above a liquid water reservoir as the origin of the South Pole hotspot on Enceladus, *Icarus*, *196*, 642–652, doi:10.1016/j.icarus.2008.03.008.
Travis, B. J., and G. Schubert (2015), Keeping Enceladus warm, *Icarus*, *250*, 32–42, doi:10.1016/j.icarus.2014.11.017.
Turcotte, D. L., R. J. Willemann, W. F. Haxby, and J. Norberry (1981), Role of membrane stresses in the support of planetary topography, *J. Geophys. Res.*, *86*, 3951–3959, doi:10.1029/JB086iB05p03951.
Tyler, R. H. (2011), Ocean tides heat Enceladus, *Geophys. Res. Lett.*, *36*, L15205, doi:10.1029/2009GL038300.
Van Hoolst, T., R.-M. Baland, and A. Trinh (2013), On the librations and tides of large icy satellites, *Icarus*, *226*, 299–315, doi:10.1016/j.icarus.2013.05.036.
Van Hoolst, T., R.-M. Baland, M. Yseboodt, and A. Trinh (2016), The diurnal libration and interior structure of Enceladus, Icarus, doi:10.1126/science.1121290, in press.
Waite, J. H., M. R. Combi, W.-H. Ip, T. E. Cravens, R. L. McNutt, W. Kasprzak, R. Yelle, J. Luhmann, H. Niemann, D. Gell, B. Magee, G. Fletcher, J. Lunine, and W.-L. Tseng (2006), Cassini ion and neutral mass spectrometer: Enceladus plume composition and structure, *Science*, *311*, 1419–1422, doi:10.1126/science.1121290.
Zolotov, M. Y. (2007), An oceanic composition on early and today's Enceladus, *Geophys. Res. Lett.*, *34*, L23203, doi:10.1029/2007GL031234.